ADVANCED MATERIALS INTERFACES
Open Access
www.advmatinterfaces.de

Nanoengineering of Chitosan Sponges Via Atomic Layer Deposition of ZnO for Water Remediation Technologies

Sara Lotito, Domenico Cignolo, Jennifer Gubitosa, Gianni Barucca, Paolo Mengucci, Marinella Striccoli, Fabio Palumbo, Pinalysa Cosma, Paola Fini, Sapia Murgolo, Vito Rizzi, Francesco Fracassi, Antonella Milella,* and Alberto Perrotta**

Low-cost, millimeter-thick chitosan-based sponges are engineered with zinc oxide (ZnO) using atomic layer deposition (ALD) to create a multifunctional nanocomposite for the potential application in water remediation and self-regeneration via solid-state photocatalysis. Initially, non-porous chitosan films served as control samples to study the ZnO growth mechanism and its impact on the biopolymer's optical and chemical properties. Subsequently, porous chitosan sponges are engineered to further explore the photocatalyst growth and infiltration into the porous matrix. The characterization of the chitosan/ZnO hybrid material is performed using spectroscopic ellipsometry, X-ray photoelectron spectroscopy, UV–vis, photoluminescence, and infrared spectroscopy, analyzing the effect of varying the number of ALD cycles, resulting in different ZnO thicknesses in the range of 5–30 nm on the chitosan matrix. A reaction-limited growth model is found and strong interactions between ZnO and chitosan amino groups significantly enhance the stability in water and impart photocatalytic features. Adsorption tests using Direct Blue 78 dye demonstrated high removal efficiency, with capacities up to 2000 mg g^{-1}, surpassing pristine chitosan sponges, which degrade in water. Electrostatic interactions between dye sulfonate groups and protonated chitosan amino moieties are identified as key to this performance. Preliminary photocatalytic experiments using Naproxen confirms the ZnO-coated sponges' ability to degrade pollutants, showcasing ALD as a key technology for producing bio-based, photoactive materials for sustainable water treatment.

1. Introduction

Over recent decades, poor water quality has become a major concern, critically challenging the scientific community. Specifically, the disposal of large quantities of undesirable substances, originating from both natural processes and human activities, often induces adverse effects closely tied to social and economic changes.[1]

Technological advances have enabled the detection of a growing number of pollutants and their by-products, which were previously undetectable in water bodies. Notably, this includes textile dyes and emerging contaminants (ECs) present in aquatic environments.[2–4] Established strategies such as adsorption, advanced oxidation processes (AOPs), and filtration techniques have been widely employed for their removal, providing effective solutions to enhance water quality.[5]

However, the adsorption process is usually considered particularly effective, especially when using bio-based adsorbents due to their low cost,

S. Lotito, D. Cignolo, J. Gubitosa, P. Cosma, V. Rizzi, F. Fracassi, A. Milella
Dipartimento di Chimica
Università Degli Studi di Bari "Aldo Moro"
Bari 70126, Italy
E-mail: jennifer.gubitosa@uniba.it; antonella.milella@uniba.it

S. Lotito, J. Gubitosa, F. Palumbo, A. Perrotta
CNR NANOTEC – Istituto di Nanotecnologia – Sede Secondaria di Bari c/o Dipartimento di Chimica
Università degli Studi di Bari "Aldo Moro"
Bari 70126, Italy
E-mail: alberto.perrotta@cnr.it

The ORCID identification number(s) for the author(s) of this article can be found under https://doi.org/10.1002/admi.202400831

G. Barucca, P. Mengucci
Dipartimento di Scienze e Ingegneria della Materia, dell'Ambiente ed Urbanistica
Università Politecnica delle Marche & UdR INSTM
Ancona 60131, Italy

M. Striccoli, P. Fini
CNR IPCF: Istituto per i Processi Chimico-Fisici – Sede Secondaria di Bari- c/o Dipartimento di Chimica
Università degli Studi di Bari "Aldo Moro"
Bari 70126, Italy

S. Murgolo
CNR IRSA – Istituto di Ricerca sulle Acque – Sede Secondaria di Bari
Bari 70132, Italy

DOI: 10.1002/admi.202400831

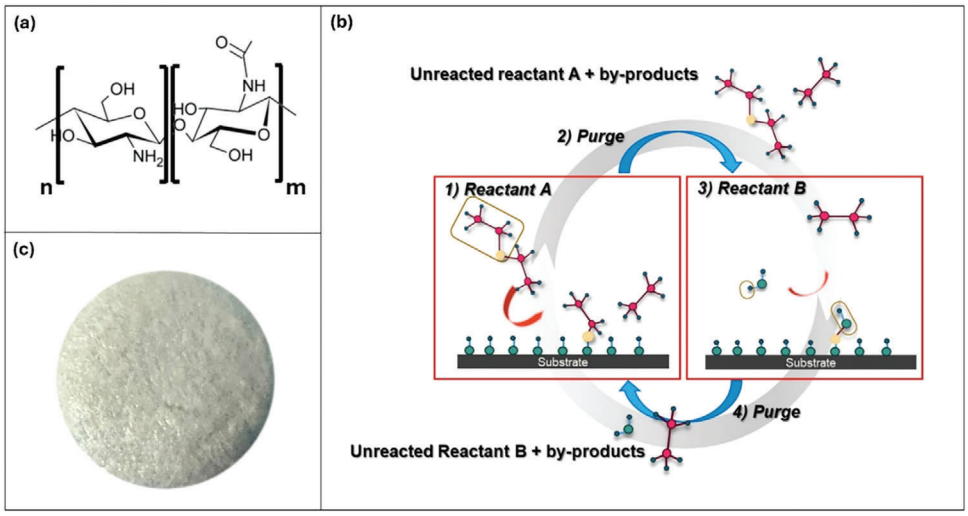

Figure 1. a) Chemical structure of chitosan; b) schematic representation of the ALD process; c) chitosan sponge.

simplicity of design, and reusability, which make them suitable for scale-up.[6] Biopolymer-based adsorbents have been employed for the removal of dyes, heavy metals, and other contaminants.[7–20] For instance, chitosan, a polysaccharide derived from crustacean shells, contains amino and hydroxyl groups (**Figure 1a**) that enhance its adsorption properties, and it has been largely used for water treatment.[21,22]

Chitosan-based adsorbents have been previously modified with metal oxides (e.g., Fe_2O_3, ZnO, TiO_2), resulting in the development of nanocomposite materials with enhanced properties, such as increased adsorption capacity, improved permeability, and photocatalytic as well as antimicrobial activities.[23–27] These hybrid nanocomposites offer multifunctionality, enabling the treatment of diverse pollutants. Furthermore, the combined use of adsorption and photocatalysis is considered an optimal strategy for water purification and adsorbent regeneration. Among various metal oxides, ZnO stands out for photocatalytic applications due to its wide direct bandgap, strong oxidative potential, cost-effectiveness, and environmental compatibility.[28]

Previous studies have reported the use of chitosan-ZnO nanocomposites, prepared by various wet methods, for the removal of dyes, drugs, and their derivatives from water (e.g., p-nitrophenol, methylene blue, ciprofloxacin, carbamazepine).[27,29–31] However, commonly used interface engineering techniques, such as physical blending, chemical grafting, and sol-gel methods, are prone to drawbacks, including coalescence, aggregation, and potential structural damage to the substrate or support. These methods can be also constrained by complexity or lengthy procedures. Furthermore, the non-uniform morphology of many adsorbents, typically characterized by a highly porous structure, necessitates the use of conformal interface modification techniques to achieve a uniform coating.[32]

In this light, atomic layer deposition (ALD) is emerging as an outstanding tool for adsorbent and membrane surface engineering due to its processing capabilities, even on complex 3D structures (Figure 1b).[33–35] By decorating the surface with photocatalytic functional nanolayers, ALD coatings can enhance the adsorption capacity and increase or even enable the adsorbent regeneration by taking advantage of the photocatalytic properties shown in the literature.[34,36] Besides, ALD-grown catalysts, such as ZnO,[37,38] TiO_2,[39] Fe_2O_3,[40] have already been applied for the purification of dyes and antibiotics containing wastewater both under UV or visible light radiation.

The chemisorptive nature of ALD allows it to potentially functionalize also biopolymers, such as chitosan, with photocatalysts. The application of ALD on polysaccharides has been mainly focused on cellulose-based materials, and only a handful of papers focus on the modification of chitin and chitosan.[41–45] Angelova et al.,[43] demonstrated that low-temperature ALD of ZnO was effective in the surface functionalization of chitosan and chitosan/hydroxyapatite composite materials for improving the bioactivity properties. Zhu et al.,[44] reported on 1D nanostructures of ZnO on carbon nanotubes/Chitosan-modified titanium by ALD with highly desirable properties in implant materials in orthodontic fields. Another use of the ALD on chitosan has been studied by Hirvikorpi et al.,[45] reporting the ALD of Al_2O_3 onto a polylactide biopolymer for food and pharmaceutical packaging.

However, there is still a gap in the current literature regarding the nanoengineering of chitosan using the ALD approach for synergistic applications in water remediation and photocatalysis. Hence, in this study, we explored the potential of chitosan thin films and porous sponges, previously investigated as adsorbents,[46–48] by applying atomic layer deposition (ALD) of ZnO. Both approaches allowed for a comprehensive evaluation of the growth mechanisms, as well as the optical and chemical properties, followed by an assessment of the sponges' adsorption capacity. Preliminary experiments on the adsorption process were conducted using Direct Blue 78 (DB), a commonly employed azo textile dye, as a model contaminant. The enhanced performance of the developed nanocomposite highlights its potential application in environmental remediation, specifically utilizing chitosan sponges.

Furthermore, to demonstrate the photocatalytic activity of ZnO, Naproxen—a persistent EC not adsorbed by the chitosan

sponges—was used in preliminary experiments. These experiments confirmed the materials ability to degrade pollutants under light exposure, showcasing the ZnO-coated chitosan as a promising photocatalytic system.

Notably, native chitosan sponges typically undergo rapid dissolution in water, reverting to a hydrogel state, which limits their direct applicability in aqueous environments. Wang et al.,[49] previously addressed this issue using highly concentrated NaOH solutions for stabilization. In contrast, our approach utilized ALD as a key enabling technology, avoiding harsh chemical treatments and achieving water-stable, photoactive organic-inorganic hybrid bio-adsorbents. This dual functionality of adsorption and photocatalysis offers a synergistic pathway for the efficient removal of pollutants from contaminated water.

2. Experimental Section

2.1. Materials

Diethylzinc (DEZ) (Strem Chemicals, Inc., min 95%, CAS 557-20-0) and Milli-Q water were used as the metalorganic and oxygen precursors, respectively, while argon (99.9%) was employed as an inert gas during the ALD process.

Commercial-grade chitosan powder (from crab shells, highly viscous, with a deacetylation degree of ≥75%), acetic acid (99.9%), and Naproxen (NAX) were purchased from Sigma–Aldrich (Milan, Italy). Direct Blue-78(DB) (Molecular Formula: $C_{42}H_{25}N_7Na_4O_{13}S_4$, Molecular Weight: 1055.91 g mol^{-1}, CAS Registry Number: 2503-73-3) was received from Colorprint Fashion, SL, and used without further purification. A DB stock solution with a concentration of 30 mg L^{-1} was prepared in deionized water and diluted as needed. All measurements were performed in triplicate, and error bars represent standard deviations.

2.1.1. Atomic Layer Deposition of ZnO

A custom-built ALD reactor was used to deposit ZnO thin films. The reactor consisted of a cylindrical stainless steel vacuum chamber evacuated by a turbomolecular (Pfeiffer Vacuum D-35614 Assalar)/rotary system (Pfeiffer Vacuum DUO 20 MC) and equipped with a resistive heating plate.

DEZ and MilliQ-water (named "Reactant A" and "Reactant B", respectively, in Figure 1b) were sequentially injected into the reactor by means of Ar as carrier gas that was continuously flowed for easier removal of by-products and unreacted precursors. The Ar flow rate was controlled by an electronic mass flow controller (MKS Instruments) and fixed at 30 sccm. The pressure in the chamber was monitored by a compact capacitive gauge (Pfeiffer Vacuum) and was set to a base value of 60 mTorr.

An ALD valve (Fitok ALD Series) was used to pulse DEZ into the reactor as well as pneumatic valves (Swagelok) for Ar and water. To avoid condensation, the water delivery line was heated to 45–50 °C, while for DEZ no further heating was necessary due to its high vapor pressure.

The ALD recipe optimized at 100 °C comprises the repetition of the following four steps 1) DEZ dose (0.15 s); 2) Ar purging (25 s); 3) water dose (6 s); 4) Ar purging (50 s) (Figure 1b). The number of deposition cycles varied between 10 and 100. The opening and closing sequences of the valves were controlled by an Arduino microcontroller and freeware Python-based software.[50]

ZnO was deposited onto silicon doubled-polished substrates with a native oxide without any further pre-treatment, onto TEM grids (Agar Scientific, carbon films on copper grids) or on glass slides (Diamond Microscope slides, 1.2 cm x 2 cm) depending on the analysis. Glass slides were ultrasonically cleaned, consecutively in acetone, MilliQ-water, ethanol and then left to dry prior to use.

2.1.2. Preparation of Chitosan Hydrogel and Sponges

Chitosan was solubilized in water to obtain a concentration of 1% (w/v) in the presence of acetic acid 0.8% (v/v). To ensure the complete polymer dissolution, the mixture was continuously stirred for 24 h. The obtained hydrogel was filtered and degassed for 1 h. Round plastic Petri plates were used as a template for forming solid-state sponges. In detail, the hydrogel was placed inside the plates and frozen for 24 h at −20 °C. The side of the sponges in direct contact with the Petri plate was called side B, the other was indicated as side A. Subsequently, the samples were freeze-dried for 24 h using a Thermo Scientific Heto LyoLab 3000 freeze dryer.

2.1.3. Preparation of Chitosan Thin Films

Chitosan thin films were prepared by spin-coating the hydrogel from which the sponges were made onto silicon doubled-polished substrates or onto glass slides (Diamond Microscope slides, 1.2 cm x 2 cm) depending on the analysis. An oxygen plasma (see Supporting Information) was adopted as a pretreatment prior to the spin-coating process.

The substrates, either glass or silicon ones, were covered with chitosan hydrogel and spun at a speed of 4000 rpm, with an acceleration of 1000 rpm s^{-1}, for 30 s.

2.1.4. Chitosan Films and Sponges Nanoengineered Via ALD

The ALD recipe for ZnO deposition was applied either on porous sponges (Figure 1c) or on chitosan thin films. The effect of the ALD cycles was evaluated in the range of 10–100 and for each deposition, a silicon slide was introduced into the reactor as control sample. The chitosan samples ALD-modified, either thin films or sponges, will be named as ZnO(**X**cy)@Chitosan, where **X** stands for the number of ALD cycles. For the chitosan sponges the side named as "A" was directly exposed to the precursors while the side B was in contact with the heating plate.

Control samples of both chitosan thin films and sponges were the ones processed without exposure to the ALD precursors (under vacuum and at 100 °C for a few hours).

2.2. Opto-Chemical Characterization

The optical properties of ZnO, chitosan thin films, and nanoengineered chitosan thin films were evaluated by spectroscopic ellipsometry (SE) analysis (J. A. Woollam Co., Inc. M-2000UI EC-400).

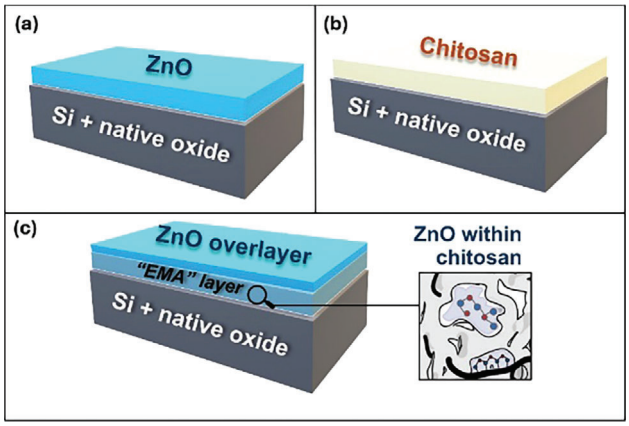

Figure 2. a) Schematic representation of the models adopted in spectroscopic ellipsometry modeling for ZnO, b) chitosan thin films c) and the hybrid material ZnO@Chitosan.

The spectra were acquired at three different angles of incidence (50°, 60°, and 70°) in a wavelength range of 250–1700 nm. The spectra were modeled with the software CompleteEASE (Version 4.92, J. A. Woollam Co., Inc.). A three-layer model, considering the Si substrate with backside reflection correction and a SiO_2 native layer with an average thickness of 1.80 nm, and ZnO layer (**Figure** 2a) and chitosan layer (Figure 2b) respectively, was used to determine the optical constants of the alone-standing materials.

For the ZnO layer, the optical constants were determined by modeling the SE spectra with a Cody Lorentz dispersion function that takes into account also the absorption at energies below the bandgap (E_g).

Then, for the chitosan layer that does not show absorption in the investigated spectral region, the Cauchy model, following this three-term equation (Equation 11), was adopted:

$$n\ (\lambda) = A + \left(\frac{B}{\lambda^2}\right) + \left(\frac{C}{\lambda^4}\right) \quad (1)$$

in which n is the wavelength-dependent refractive index, λ is the wavelength and A, B, and C are fit parameters.

The spectra of the hybrid material were modeled by adopting a four-layer model reported schematically in Figure 2c which consists of the Si substrate with backside reflection correction, a SiO_2 native layer with an average thickness of 1.80 nm, an "Effective Medium Approximation" layer (EMA) and the ZnO overlayer. Specifically, considering the chitosan thin films as a matrix with a free volume that could be filled by ALD precursors, the EMA model was employed in ellipsometric data analysis. This modeling approach was typically adopted to calculate the optical constants of a mixed material as well as the percentage of inclusion of one of the constituents. The pre-determined optical constants of the ZnO and chitosan films were incorporated into the EMA model as the fitting starting point. For the ZnO overlayer thickness determination, the Cody–Lorentz dispersion function was used.

UV–vis spectra were collected by using Agilent Technologies Cary 60 UV–vis (wavelength range: 200–800 nm) of ZnO thin films, chitosan thin films, and the ALD-modified ones. UV–vis spectrum was collected also for the chitosan thin film adopted as the control sample.

Photoluminescence (PL) measurements were made at room temperature and the spectra were recorded with a Fluorolog 3 spectrofluorometer (HORIBA Jobin-Yvon GmbH, Bensheim, Germany) equipped with a 450 W Xe lamp as excitation source, with double grating excitation and emission monochromators and a TBX single photon counter as detector. PL measurements were performed on ZnO deposited on Si substrates and on chitosan thin films both before and after ALD-nanoengineering. The selected excitation wavelength at 350 nm allowed the measurement of the ZnO band edge-related photoluminescence (Eg = 3.37 eV for bulk ZnO at room temperature).

The surface wettability of the ZnO thin films deposited on silicon slides was probed by static water contact angle (WCA) measurements with a Rame´- Hart NRLgoniometer (MilliQ water, 1 uL drops, room temperature).

Fourier-Transform Infrared spectroscopy (FT-IR) analysis was adopted to investigate the chemistry of the ZnO thin film. The spectrum was collected, under mild vacuum, in the range of 400–4000 cm^{-1} over 32 scans. The spectrum was baseline-corrected and normalized to its thickness.

Attenuated total reflectance (ATR)-FT-IR analyses were performed on chitosan sponges before and after the ALD cycles, investigating the effect of ZnO deposition. Measurements, after the adsorption of the dye were also performed to better investigate the nature of the interaction between the adsorbent and the pollutant. The spectra were recorded in a 450–4000 cm^{-1} range over 16 scans, at a resolution of 4 cm^{-1}, using an FT-IR Spectrum Two from Perkin Elmer, Waltham, MA, USA.

X-ray Photoelectron Spectroscopy (XPS) was carried out by using a PHI VersaProbe II (PhysicalElectronics GMBH) equipped with a monochromatic Al Kα X-ray source (1486.6 eV), operated at 15 kV and 24.8 W, with a spot of 100 μm. Prior to the analysis, the ZnO thin films were "'in situ"' argon sputter-cleaned using an Ar^+ ion beam. To assess ZnO infiltration, XPS depth-profiling analysis was carried out on both chitosan thin films and sponges, with the latter being more interesting for the proposed application. High-resolution (HR) spectra elaboration was performed with MultiPak (Physical Electronics) data processing software.

2.3. Structural, Morphological, and Thermal Properties Characterization

Structural and microstructural investigations were performed by X-ray diffraction (XRD) and Transmission Electron Microscopy (TEM). XRD measurements were conducted to assess the crystallinity of both ZnO thin films as well as of the ZnO grown on/within chitosan by using a Bruker D8 Advance diffractometer (Karlsruhe, Germany), operating with a Cu-Kα radiation in the angular range $2\theta = 10 - 80°$. In order to evidence even the less intense peak, the ZnO thin film analysis was performed in the angular range $2\theta = 30 - 38°$, and patterns were plotted in square root full-scale intensity. Peak identification was carried out by using DIFFRAC.EVA software package including ICDD—PDF 2 database.

TEM measurements were carried out in a Philips CM200 electron microscope operating at 200 kV. The samples were prepared

by scraping small amounts of powder from the surface of chitosan sponges onto carbon-coated copper grids. The grids were previously covered with a small drop of ethanol to enhance the adhesion and spread of the sponge powder on the carbon film during the following ethanol evaporation.

The thermal properties were investigated using a thermogravimetric analyzer (Perkin Elmer Pyris 1), working under a nitrogen flow of 30 mL min^{-1} at a heating rate of 10 °C min^{-1}. The thermogravimetric (TG) experiments were performed from 35 to 600 °C.

2.4. Swelling, Adsorption and Photocatalytic Properties

The chitosan sponges, before and after the ALD cycles, were subjected to swelling measurements. For this purpose, the sponges were weighted and swollen in bi-distilled water, at controlled room temperature. Specifically, the measurements of weight were performed every minute until the equilibrium was attained. The sponges were blotted with filter paper and weighed. To infer the swelling percentage Equation (2) was used.[51]

$$\%\ \text{Swelling} = \frac{W_s - W_d}{W_d} \times 100 \quad (2)$$

where w_s is the weight of the swollen sponge at time t and w_d is the weight of the dried sponge.

UV–vis spectra were recorded using a Varian CARY 5 UV–vis-NIR spectrophotometer (Varian Inc., now Agilent Technologies Inc., Santa Clara, CA, USA). Spectra were recorded in a 200–800 nm range, at a 1 nm s^{-1} scan rate, and the dye DB amount in water was monitored by measuring the absorbance intensity at $\lambda = 605$ nm. The following molar absorption coefficient (ε) was used, 22 000 L mol^{-1} cm^{-1}, to infer the dye concentration.

The adsorption capacities (q_t, mg × g^{-1}) of the proposed adsorbents, at different contact times, were calculated by using Equation 3.[52,53]

$$q_t = \frac{C_0 - C_t}{W} \times V \quad (3)$$

where V represents the volume of water containing the pollutant DB at a concentration of 25 mg L^{-1} (in 15 mL), W is the amount of adsorbent (g), and C_0, C_t, are the contaminant concentrations (mg L^{-1}), calculated at time, t_0, and at generic time, t, respectively. In detail, 3 mg of adsorbents were placed in water polluted with DB and monitored until the equilibrium condition was reached.

A UV lamp (UV fluorescent lamp, Spectroline, Model CNF 280C/FE, $\lambda = 254$ nm, light flux 0.2 mW cm^{-2}; USA) was used to irradiate the sponge proposed as photocatalytic solid support to induce the degradation of pollutants on its surface. The adsorbent was placed in properly contaminated water (15 mL) by NAX adopted as a model contaminant and exposed to UV light for 60 min. At the end of the experiments, the concentration of the pollutant in water was inferred by using UV–vis spectroscopy.

2.5. Analytical Determination of Photoproducts and Data Processing

An Ultimate 3000 System (Thermo Fisher Scientific), interfaced with a TripleTOF 5600+ high-resolution mass spectrometer (AB-Sciex) equipped with a duo-spray ion source operating in positive electrospray mode (UPLC-ESI-QTOF-MS/MS), was used to identify the photoproducts produced by Naproxen photodegradation.

Samples collected at different irradiation times (0, 2, and 4 h) during the photocatalytic experiment with ZnO-coated sponges were analyzed using an optimized analytical method. The following mass spectrometry (MS) operating conditions were employed: curtain gas (20 psig), ion source gas 1 (nebulizer gas, 35 psig), ion source gas 2 (turbo gas, 45 psig), IonSpray voltage (5500 V), source temperature (500 °C), declustering potential (80 V), collision energy (35 V), and collision energy spread (15 V). All MS analyses were performed using a double-experiment acquisition method—full-scan survey TOF-MS combined with an IDA (Information Dependent Acquisition) experiment—scanning a mass range from 50 to 600 m z^{-1}.

A ZORBAX Eclipse Plus C18 column (150 × 2.1 mm, 1.8 µm) operated at a flow rate of 0.300 mL min^{-1} was used to achieve chromatographic separation of the analytes. A 50 µL aliquot of each sample was injected and eluted with a binary gradient composed of 0.1% formic acid in water (solvent A) and 0.1% formic acid in acetonitrile (solvent B), as follows: starting at 2% B, linearly increasing to 20% B over 1 min, then to 100% B over 10 min, and maintained at 100% B for 3 min. A 4-minute equilibration step at 2% B was employed at the end of each run.

The collected data files were qualitatively processed using AB Sciex's MetabolitePilot software. Briefly, the software's approach relies on a predefined list of common transformation reactions (e.g., decarboxylation, demethylation, oxidation, hydrogenation, etc.) that allows for the prediction of potential cleavage products starting from the parent compound Naproxen. The software identifies possible products by comparing the accurate masses of the detected molecular ions with the accurate mass of the Naproxen molecular ion. If the mass shift corresponds to one of the listed transformation reactions, the software assigns the corresponding reaction name to the predicted product and provides a potential formula, isotopic pattern, retention time, and detailed MS/MS spectral information.

3. Results and Discussion

3.1. Atomic Layer Deposition of ZnO and Nanoengineering of Chitosan Thin Films

The properties of the ZnO (250 cycles, 47 nm thick), deposited at 100 °C using the optimized recipe, were first investigated to highlight the differences in growth on typical ALD optimization substrates (e.g., Si substrate, glass slide) compared to chitosan. The refractive index and extinction coefficients, modeled from the SE data of the as-grown ZnO film, are reported in **Figure 3a**.

The refractive index of the film at 632.8 nm on the Si substrate is 1.916 ± 0.001, which is lower than that of ZnO single crystals (1.99).[54] However, this value is consistent with other reports for ZnO films grown via ALD[55] and plasma-enhanced atomic layer deposition (PE-ALD).[56] Figure 3b presents the UV–vis spectrum of the ZnO thin film, showing a bandgap of 3.21 ± 0.06 eV, as determined by the Tauc plot. This bandgap is slightly lower than the reported value for ZnO single crystals (3.3 eV)[57] but aligns with values observed for ZnO thin films,[58,59] grown using either PE-ALD[60] or ALD.[61] The bandgap value obtained from

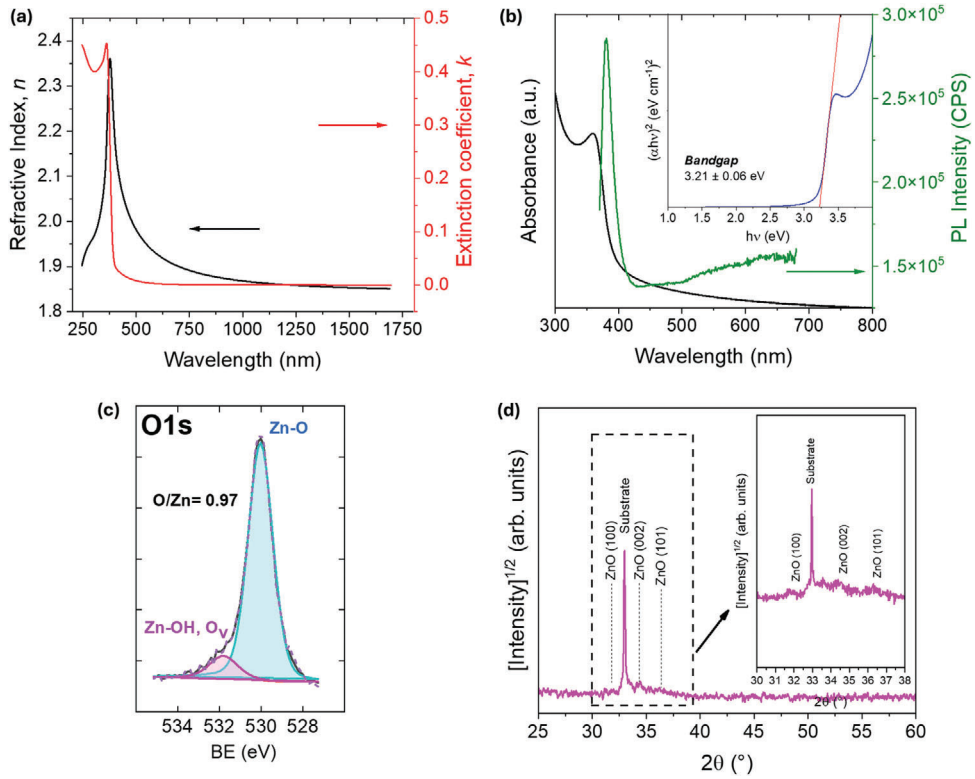

Figure 3. Physical-chemical properties of ALD ZnO thin films deposited at 100 °C. a) Refractive index and extinction coefficient derived from SE modelling for 47 nm-thick ZnO thin film; b) UV–vis absorption and PL spectra (excitation wavelength: 350 nm). The inset shows the bandgap determination of ZnO thin film; c) XPS O1s peak with the relative O/Zn ratio; d) XRD pattern of the ALD ZnO thin film grown on Si. The inset shows a restricted range of the pattern (30–38°).

UV–vis analysis is corroborated by SE, which measured a bandgap of 3.25 ± 0.18 eV, demonstrating the robustness of the ellipsometric optical model used.

In Figure 3b, the film exhibited strong light absorption in the UV region, with a characteristic free exciton peak at 360 nm, indicating the high-quality nature of the thin film.[62] This finding was further supported by the sharp and intense near-band edge (NBE) excitonic emission observed at ≈380 nm in the PL spectra, which typically arises from high-quality hexagonal wurtzite ZnO.[61] The ZnO film displayed also a broad and low-intensity emission in the red region. In the literature, the peak ≈640 nm was attributed to surface defects linked to an excess of surface oxygen or the presence of interstitial oxygen, which can introduce acceptor states above the valence band. The high-intensity ratio between the band-edge emission and the defect band further confirmed the optical quality of the deposited ZnO layers. Saha et al.,[63] reported that ALD ZnO deposited at different temperatures exhibited two broad emissions: one ≈490 nm (green emission), attributed to oxygen vacancy-related point defects, and another at 590 nm (orange emission), associated with an excess of hydroxyl (—OH) groups. In this context, our PL measurements (Figure 3b) highlighted the presence of —OH-related defects. This finding was further confirmed by XPS analysis, where the best fitting of the O1s peak indicated a component at 531.8 eV (Figure 3c), which was attributed to zinc hydroxides and/or defective oxygen,[64,65] whereas the low binding energy component corresponds to oxygen in the zinc oxide lattice.[66,67]

The high quality of the material was further supported by the high crystallinity assessed by XRD measurements for ZnO deposited on Si (Figure 3d). It was found that ZnO thin film is polycrystalline with a hexagonal wurtzite structure. Three broad and low-intensity XRD peaks were identified, i.e., (100), (101), and (002) indicating that the film is composed of a mixture of grains both with c-axis parallel and perpendicular to the substrate surface which is common for a relatively low-temperature range ALD-grown ZnO.[68,69]

On the other hand, the Zn2p$_{3/2}$ (Figure S1, Supporting Information) clearly displays a single and symmetric peak at 1021.4 eV referred to as the ZnO.[66] The presence of —OH moieties was confirmed by FT-IR spectra as indicated by the broadband in the range of 3000–3600 cm^{-1}.[70] Thus, the ZnO defective states, either stemming from oxygen vacancies or hydroxyl groups, may account for the SE-measured refractive index, pointing out a lower mass density. A sharp absorption band at ≈407 cm^{-1} corresponding to the Zn—O stretching vibration for the tetrahedral surroundings of zinc atoms[71,72] was also observed.

To investigate the quality and growth of ALD ZnO on the surface of chitosan, chitosan thin films spin-coated onto Si substrates were used as a model, enabling the use of a broader range of characterization methods. SE, UV–vis spectroscopy, and PL were employed to determine the optical properties of the grown ZnO, as well as to track the evolution of these properties with the number of ALD cycles. The SE spectra for chitosan thin films

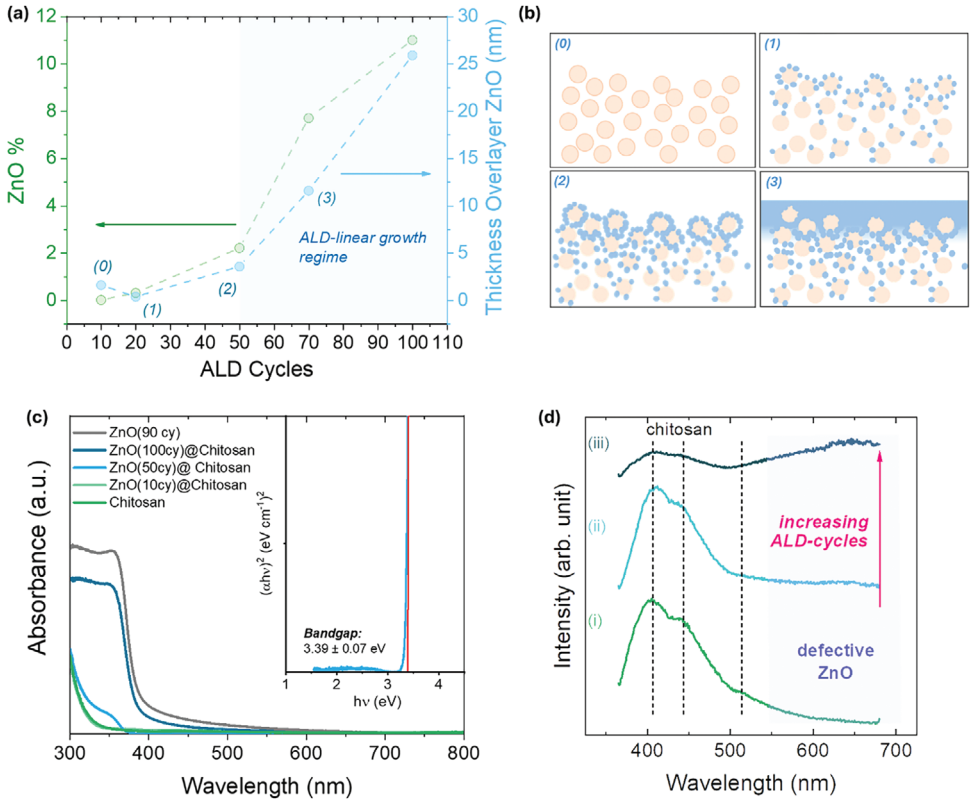

Figure 4. a) ZnO (%) infiltrated within the polymeric matrix derived from the EMA model and thickness of the ZnO overlayer as a function of ALD cycles.; b) Schematic representation of the growth of ZnO on/within the polymeric matrix, represented as loosely packed circles (0), and the relative steps: infiltration and surface reaction of DEZ and water 1), pore size reduction with the increasing of ALD cycles, 2) formation of a continuous overlayer 3). Image readapted from Wilson et al.,[75] reflecting the growth model suggested for ALD ZnO on chitosan thin films; c) UV–vis absorption spectra of ZnO@Chitosan as a function of ALD cycles compared to the bare ZnO and chitosan thin film. The inset shows the bandgap determination for ZnO(50cy)@Chitosan d) PL spectra of i) chitosan thin film and ii) ZnO(50 cy)@Chitosan and iii) ZnO(100 cy)@Chitosan (excitation wavelength: 350 nm).

and ZnO-modified ones were acquired and fitted according to the optical model reported in the Experimental Section. SE can be used to monitor the changes in the optical properties and thickness (i.e., the optical density) occurring upon exposure to the ALD precursors, as also reported for sequential infiltration synthesis (SIS) and vapor phase infiltration (VPI).[73,74] The infiltration extent can be retrieved from the combinatorial sum of the optical properties obtained by the EMA layer. Thus, once the optical properties of ZnO were determined, the thickness of the chitosan thin films assumed as control samples were acquired, which ranged between 120 and 296 nm.

By adopting the optical properties of both bare ZnO and chitosan thin films control samples, it was possible to model the amount of ZnO included in the polymeric matrix as reported in **Figure** 4a whereas the corresponding equivalent thickness is shown in Table S1 (Supporting Information). The percentage of ZnO within the EMA layer was found to increase as a function of the ALD cycles being an indication that infiltration occurred. Thus, by comparing the refractive index values reported in **Table** 1, a clear densification took place as a function of the number of cycles.

The growth of the ZnO on top of the chitosan thin film was determined and reported in Figure 4a.

Table 1. Refractive index values determined by SE of ZnO@Chitosan as a function of ALD cycles compared to ZnO and chitosan thin film.

Sample	n@632.8 nm [± 0.001]
Chitosan	1.512
ZnO(10 cy) @Chitosan	1.515
ZnO(50 cy)@Chitosan	1.518
ZnO(100 cy)@Chitosan	1.521
ZnO (250 cy)	1.916

The results suggest that at the early stages of deposition, both top surface reactions and infiltration in the near-surface region occurred, with the latter being the predominant process. From the 50th cycle onward, the top ZnO layer began to exhibit linear growth, and the modeled infiltration increased by up to 11%. We hypothesize that as the infiltrated ZnO in the near-surface region continues to grow, the progressive exposure to DEZ and water may lead to the filling of the free volume between the polymer chains. Consequently, starting from the 50th cycle, a continuous overlayer is predominantly formed. The infiltration and subsequent linear growth resembled the growth model reported

by Wilson et al.[75] for Al_2O_3 ALD on spin-coated polymer films (such as PE, PS, PVC, PMMA, PP). According to this study, the nucleation may differ between the polymers due to different diffusion rates and retention which are correlated with the free volume and the solubility of the precursor in the polymer film, respectively. However, following the initial nucleation period, a linear growth was observed on all the polymers. In this light, a fairly general model in explaining Al_2O_3 growth on/within different polymers has been proposed and well applies to the ZnO-on-chitosan presented in this work (Figure 4b).

XPS-depth profile analysis allowed the assessment of the formation of a continuous overlayer at 100 cycles and that infiltration took place within the polymeric matrix in the first 10–20 nm (Figure S2, Supporting Information). Herein, based on these findings, we believe that also the current case study follows the above-mentioned growth model proposed.

The optical characterization was performed also via UV–vis absorption of both pristine and nanoengineered chitosan thin films and ZnO. As can be observed in Figure 4c, when a continuous layer of ZnO is deposited onto chitosan thin films (achieved in the reported case at 100 cycles), the absorption peak loses the excitonic peak, suggesting the growth of ZnO with a poorer quality. Nevertheless, the bandgap (3.29 ± 0.04 eV) and overall intensity are not so far from the bare ZnO ones. For this reason, we could not exclude that the signal is mainly attributed to the ZnO top layer.

Compared with the pure chitosan, by decreasing the number of ALD cycles to 50, a significant blueshift was witnessed, which resulted in a bandgap value of 3.39 ± 0.07 eV. As previously assessed via SE, up to 50 cycles, the infiltration continues, and no additional top surface growth was witnessed. Considering that a limited amount of ZnO was grown as a top layer, we assume that the bandgap is attributed to the infiltrated ZnO in the chitosan matrix. In the literature, a similar blueshift was reported for chitosan/nano-ZnO composite membranes.[76] In particular, according to the Kubo theory,[77] the absorption band would be blue-shifted with the decrease of the nanoparticles diameter. Decreasing further the ALD cycle number (10 cycles of ZnO), no photoactive material could be detected since there is no variation compared to the spectra of the chitosan thin film.

The PL measurements, reported in Figure 4d, pointed out the highly defective nature of the ALD-grown ZnO on chitosan. The pristine chitosan thin film displayed three emission bands at 408, 444, and 512 nm. However, when the chitosan thin film was subjected to the ALD nanoengineering, a broad emission from ZnO defects arose in the visible region, being more evident by increasing the amount of the grown ZnO and confirming the poorer quality of the ZnO grown on chitosan.

XRD measurements of the ALD-nonengineered chitosan thin films (Figure S3, Supporting Information), revealed the amorphous nature of the ZnO, and no crystallinity was observed for the pristine chitosan. The absence of extended crystallinity or nano-sized crystals in an amorphous matrix of ZnO is reported to still have photocatalytic activity, as for this material the disorder-degree of the amorphous oxide impacts in a negligible way the bandgap and the optoelectronic properties.[78]

In summary, the ALD ZnO classically optimized on flat and amorphous inorganic substrates indicated the production of a high-quality material at 100 °C. Conversely, the opto-chemical study of the growth of ALD ZnO on a spin-coated chitosan thin film highlighted sub-infiltration of the ZnO into the amorphous polymeric matrix, inducing a low-quality ZnO growth for the thickness explored. Similar results were reported for PE-ALD of ZnO on polymeric thin films, confirming the defect-induced initial growth affecting the quality of the deposited material.[79]

3.2. Nanoengineering of Chitosan Sponges

Once the optochemical properties of ZnO and ZnO@Chitosan thin films were assessed, to study the effect of ALD cycles on the proposed material (mm-thick chitosan sponges), the same process was applied and studied as a function of the number of cycles. ATR-FT-IR analyses were performed on both sides of the material, for simplicity only side A is reported in **Figure 5a** (for side B see Figure S4, Supporting Information).

As a first step, the pristine chitosan sponges were characterized, and the typical signals of the polymer were observed. Important changes were not detected between sides A and B. In detail, the amide I band referred to —NHR—CO— stretching, and the overlapping of the amide II band vibration (—NH_2 bending) with the carboxylate stretching of acetate anions were detected at 1640 and 1541 cm^{-1}, respectively. The broadened band, in the range 3300–3400 cm^{-1}, can be ascribed to the contribution of the O—H and N—H stretching; the doublet at 2923/2875 cm^{-1} indicated the symmetric and asymmetric C—H stretching. At 1410 and 1378 cm^{-1}, the presence of acetate anions and C—N bond peaks were also observed, respectively. The C—O—C asymmetric and symmetric stretching can be ascribed to signals at 1151 and 1059 cm^{-1}, with a band at 1031 cm^{-1} due to the C—O vibration of the alcoholic moieties.[80]

After the growth of ZnO via ALD the ATR-FT-IR profile showed some important modifications attributed to amide I and II signals at 1640 and 1541 cm^{-1}, N—H, O—H stretching in the range 3300–3400 cm^{-1}, C—H stretching at 2923/2875 cm^{-1}, and the C—O vibration at 1031 cm^{-1}. Specifically, the signals at 1640 and 1541 cm^{-1} reversed their relative intensity: the amide I band occurred more intensely with respect to amide II which seemed to reduce its contribution. Interestingly, this finding was found more pronounced with the increase of the ZnO cycles. As observed in the literature,[29] this finding can be attributed to the different protonation degrees of chitosan amino groups, and a new arrangement of chitosan array forming novel H-bonds. By considering these changes, it should be possible to assess the presence of interaction between the growing ZnO and the chitosan amino and hydroxyl functional groups. A novel chitosan network was formed, and accordingly, the signals at 1031 and 1059 cm^{-1} appeared affected, reversing their relative intensity; so, the chitosan chains reorganized, forming new H bonds and a coordination of —OH with ZnO could also be measured. Consequently, the C—H signals at ≈2900 cm^{-1} shifted toward lower wavenumbers, and the two signals clearly detected in chitosan at 2923/2875 cm^{-1} appeared as a broad peak. Not surprisingly, the whole intensity of spectra appeared reduced with the increase of the number of ALD cycles, denoting that the presence of ZnO favored a new entanglement of chitosan chains into a more rigid structure, reducing their vibrations. At the same time, it is not possible to exclude that, at the increase of the ZnO layer, the

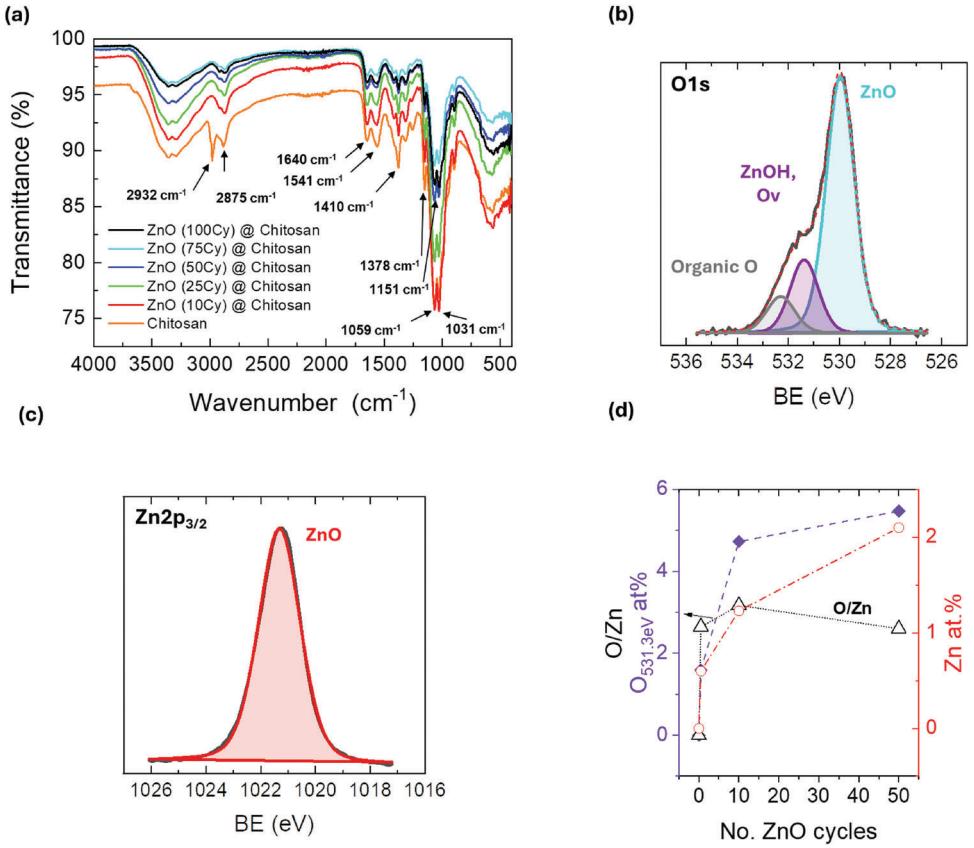

Figure 5. a) ATR-FT-IR spectra of chitosan and ZnO modified sponges referred to sides A; XPS O1s b) and $Zn2p_{3/2}$ signals c) of ZnO(100cy)@Chitosan; (d) zinc and oxygen component at 531.3 eV, usually attributed to Zn-OH, atomic percentages, and O/Zn atomic ratio as a function of ALD cycles.

chitosan vibrations should be shielded, reducing their intensity. It is worth mentioning that the detected changes in the ATR-FT-IR profiles were the same on both surfaces of the sponges, suggesting that the treatment via ALD was uniform, and involved the whole sponge thickness.

XPS was carried out to investigate more about the quality of the ZnO grown on chitosan sponges. In Figure 5b,c the O1s and $Zn2p_{3/2}$ XPS signals are reported for 100 cycles of ALD ZnO on chitosan sponges. The O1s peak was best fitted in three distinct components: organic oxygen (532.1 eV), Zn hydroxides and/or defective oxygen (531.3 eV), and O—Zn lattice bonds (529.9 eV). The $Zn2p_{3/2}$ spectrum showed a peak located at 1021.3 eV that was attributed to Zn^{2+} in ZnO.[81,65]

The C1s signal (Figure S5, Supporting Information) shows three components. The peak located at 284.8 eV is assigned to C—C/C—H bonds whereas the one at 286.5 eV corresponds to C—O bonds. Instead, the high-energy component at 288.9 eV is indicative of the presence of carboxylic/amidic groups.[82–84]

To follow the growth as a function of the ALD cycles, XPS measurements were carried out for half cycle (DEZ only exposure) 10 cycles, and 50 cycles (Figure 5d). In the O1s spectra, only the component at 531.3 eV was found, which was attributed to Zn—OH. By reporting the percentage of $O_{531.3\ eV}$ components as a function of the ALD cycles, a rapid increase was found in the first ten cycles, conversely, a relatively low atomic percentage of Zn was found, resulting in a high O/Zn ratio. The high $O_{531.3\ eV}$ atomic percentage may be primarily due to defective states especially Zn—OH ones, as previously stated, and their involvement in hydrogen bonding formation with the substrate making them less available for the reaction with diethylzinc and water and changing the O chemical environment, shifting the binding energy to lower values. After 100 ALD cycles, with the formed overlayer, a nearly stoichiometric ZnO was deposited with an O/Zn atomic % ratio of 1.1.

To better study the interface with the underlying chitosan and zinc oxide the N1s region before and after ALD-nanoengineering were compared (**Figure 6**a,b).

The N1s spectra of the pristine chitosan sponge (Figure 6a) required two components for the best curve fit located at 399.4 eV, referring to the nitrogen atom in the NH_2 group and a less intense peak at 401.2 eV related to protonated amine groups, respectively.[85,86] The amide moiety that was witnessed by FT-IR spectroscopy generates a component ≈400 eV[85] but it cannot be unambiguously distinguished due to resolution limitations.

The solubility of the pristine chitosan sponge is pH dependent, and the presence of the protonated amines leads to its dissolution hindering the application as sorbent. Upon application of the ALD ZnO layer, the ratio between the peak area of the protonated amine and amine components (Figure 6c) decreased by increasing the number of cycles, while the atomic percentage of N remains unchanged. Besides the expected reaction with the present nucleophile species such as amine and hydroxyl groups, as

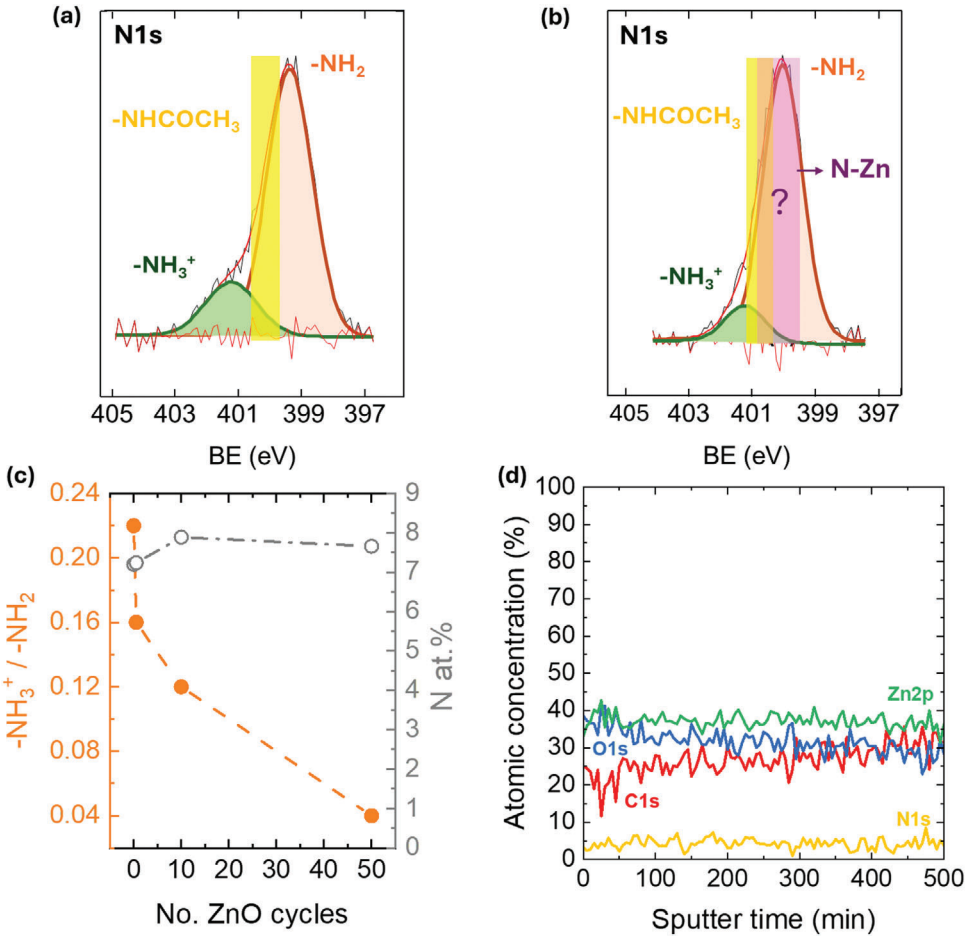

Figure 6. XPS N1s signal of chitosan sponge a) before and b) after 10 ALD cycles. Yellow and pink colors highlight the theoretical position of amide and N—Zn, respectively. c) protonated to unprotonated amine intensity ratio as a function of ALD cycles; d) XPS-depth profile analysis of ZnO(100cy)@Chitosan sponge.

previously revealed by ATR-FT-IR spectra, these results suggested that diethylzinc reacted with the protonated amines by involving them in a proton transfer step in the ligand-exchange reaction leading to —N—Zn bonding formation. The peak area intensity ratio even after a half ALD cycle, corresponding to the solely DEZ exposure, corroborated this theory and suggested that it may be a preferential site of anchoring of the growing ZnO. Something similar was reported by Perelshtein et al.,[87] in ultrasound-deposited ZnO-Chitosan composites, where the decreased intensity of the 401.9 eV peak was accounted for by the complexation between zinc and chitosan amino groups.

Moreover, since the atomic percentage of nitrogen is constant by increasing the ALD cycles, we could infer that the reduced intensity of both the component at higher and lower binding energy, related to the different protonation states of chitosan amino groups, may be followed by the rising of a new component referred to —N—Zn bonding (Figure 6b). However, this component would be hidden by the component attributed to the amine moiety. A similar conclusion was reported for polyaniline/ZnO hybrid systems via VPI.[88]

To assess the ZnO overlayer formation also on chitosan sponges, the survey spectra of the pristine chitosan sponge as well as of the modified ones were acquired (Figure S6a,b, Supporting Information). Figure S6a (Supporting Information) shows the signals of C, O, N, and a small contamination of Cl. When ALD ZnO is deposited on the chitosan sponge, Zn-related peaks are present, and their intensity increases with the ALD cycles. However, the underlying chitosan polymer remains visible up to 50 cycles, indicating the absence of a continuous ZnO overlayer at the surface with a thickness higher than the depth probing limit of XPS.

After 100 ALD cycles, the N1s peak is no longer visible, pointing out to the formation of a continuous ZnO overlayer also for the chitosan sponges (Figure S6b, Supporting Information) which has been previously predicted by the model adopted to fit the SE spectra and confirmed by the XPS depth profile analysis of the chitosan thin films.

The XPS depth profile analysis (Figure 6d) revealed that ZnO infiltration extended into the sponge matrix up to at least several tens of micrometers, effectively transforming the chitosan sponges into a hybrid organic–inorganic material. The atomic concentration profiles remained consistent across the depth, indicating uniform infiltration. This suggests that the precursor molecules were able to diffuse throughout the sponge

structure, likely reacting preferentially with protonated amine groups, which are less abundant than the amine and hydroxyl moieties. Based on these observations, it can be concluded that the current ALD process operated in a reaction-limited regime.[89]

As it was previously discussed, the bare ZnO was found polycrystalline on Si substrates and amorphous on chitosan thin films. The XRD measurements were performed also on nanoengineered chitosan sponges confirming the results obtained for chitosan thin films (Figure S7, Supporting Information). This finding is further supported by the TEM results reported in Figure S8 (Supporting Information) where the high-surface area of the sponges is highlighted, with no evidence of crystallinity. In the literature, chitosan-decorated nanotubes systems processed with ALD ZnO were found crystalline, due to the higher processing temperature and less temperature-labile substrate, together with the crystalline nature of the nanotubes.[35]

3.3. Swelling Measurements

The swelling measurements of the sponges before and after the ALD cycles were performed to evidence the reduced hydrophilic character of the adsorbent, pointing out its extended stability in water. It is worth mentioning that the chitosan swelling ability in water is well known in the literature,[80,90] and as previously discussed, it has been related to the protonation degree of the chitosan amino groups. Specifically, the greater the protonation degree, the greater the chitosan swelling. Indeed, the positively charged amino groups repel each other, favoring the formation of water channels, and enhancing the swelling of the chitosan in water. So, the sponges were placed in water to observe their behavior, and the quantitative information was obtained by applying Equation (1). Figure S9 (Supporting Information) reports the obtained results. When a sponge without ALD cycles was swollen in water, the swelling largely increased in the first minutes and leveled off after 10 min at 8000% with respect to its initial weight. As expected, the chitosan sponge is highly hydrophilic, and the structure returned in the form of a hydrogel after 15 min of contact time and was stable for 60 min. On the other hand, when testing the ALD ZnO-modified samples, the percentage of swelling reduced to ≈2000% for 10 cycles, and that value seemed to be dependent on the number of ALD cycles. Indeed, by increasing the ZnO thickness, the swelling slightly decreased. In the presence of the ZnO (75cy)@Chitosan and ZnO (100 cy)@Chitosan, the swelling collapsed to ≈1000%, suggesting the higher stability in water of these sponges with respect to those obtained with the pristine chitosan. On this ground, by considering that the swelling of the polymer is strictly related to its protonation degree, the finding suggested that ZnO reduced the hydrophilic character of chitosan, interacting, as already known in the literature, with its amino groups, screening their positive charges[29] and corroborating the mechanism previously proposed.

3.4. TG Analyses

TG analyses were performed to infer information about the thermal stability of the realized adsorbents. The results are reported in Figure S10a (Supporting Information), showing also the differential thermogravimetric (DTG) profiles to better appreciate the differences between the investigated samples (Figure S10b, Supporting Information). In this case, to better evidence the effect of ZnO deposition, a comparison was performed with the pristine chitosan sponge and the ALD-modified adsorbent. As can be clearly evidenced in Figures S10a,b (Supporting Information), pristine chitosan sponges, although subjected to the lyophilization process, presented a loss of water at ≈50 and 120 °C attributed to free and bound water, respectively.[29] The loss of weight at 323 °C can be ascribed to the polymer degradation. On the other hand, the ALD-modified sponge (in the figure indicated as chitosan and superimposed to ZnO (10 cy) @Chitosan showed only a slight loss of water, and the finding can be attributed to the used condition of work. At the same time, the degradation of chitosan occurred shifted at a higher temperature value, 330 °C. Probably, the further removal of water compacted the chitosan network increasing its thermal stability. The thermograms of chitosan sponges after the ALD cycles appeared without important changes, suggesting that the presence of ZnO did not affect the thermal features of the polymer. Indeed, two main signals were detected in Figure S10b (Supporting Information): i) an initial and slight weight loss that started at ≈50 °C and ended at ≈100 °C, attributable to the water loss; ii) a broad peak at 330 °C, corresponding to the thermal decomposition of chitosan.

3.5. Preliminary Evaluation of the Adsorption Capacity: The Direct Blue-78 Case Study

To evaluate the performance of the proposed material, preliminary adsorption experiments were conducted. Specifically, the removal of Direct Blue (DB), used as a model textile dye, was investigated. UV–vis absorption spectroscopy was used as a powerful tool to monitor its presence in contaminated water. Indeed, DB has a characteristic and intense band in the visible region of the spectrum (see **Figure** 7a), attributed by Rizzi et al. to a π–π^* transition having a charge transfer character.[91–93]

This band was thus considered diagnostic in this work to assess the presence of the dye in water. To investigate the effect of ALD cycles on the adsorption process, a comparison was made between chitosan sponges before and after ZnO deposition. For this purpose, sponges were subjected to varying ALD cycles: 10, 50, and 100. The performance of these samples was assessed against a pristine chitosan sponge and expressed in terms of adsorption capacity (q_t), with the results presented in Figure 7b. The ALD-modified sponges exhibited an increased dye removal capacity across all tested conditions compared to the pristine chitosan sponge. Notably, after just 15 min of contact with the dye solution, the pristine sponge reverted to a hydrogel state, showing limited dye adsorption. After 60 min, the hydrogel had completely dissolved in water.

Conversely, the application of the ALD ZnO layer significantly enhanced adsorption capacity. After 60 min of contact time, the q_t value increased from 20 mg g^{-1} for the pristine sponge to ≈100 mg g^{-1} for the ZnO-coated sponges. As shown in Figure 7b, no significant differences were observed in the adsorption capacities among the ALD-modified sponges with different cycle counts. The presence of ZnO not only reduced the swelling of

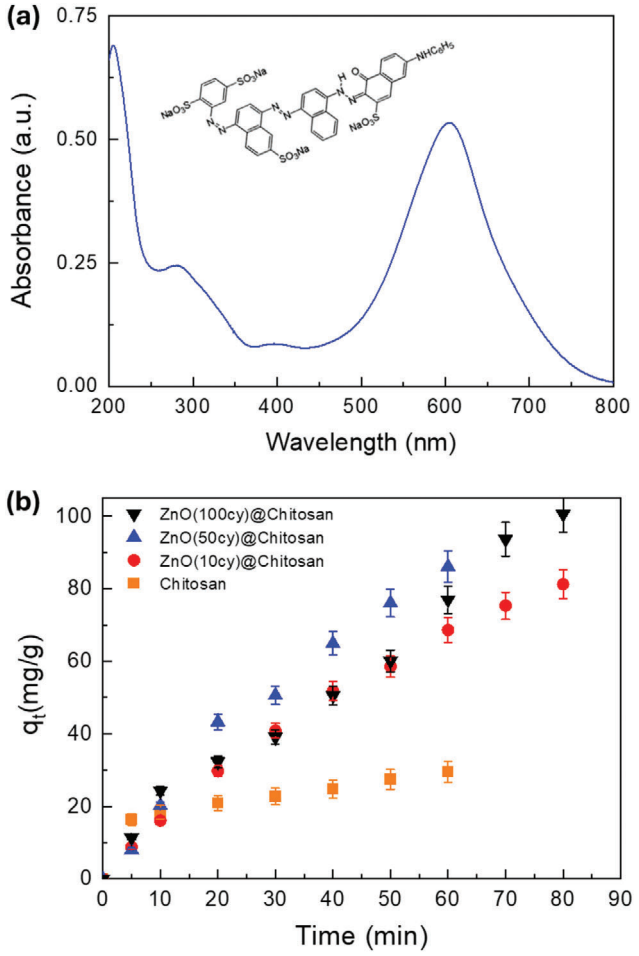

Figure 7. a) UV–vis spectrum of DB water solution and its molecular structure; b) adsorption capacities, at several contact times, referred to chitosan and ZnO modified sponges.

the sponges in water, thereby increasing their stability but also greatly enhanced the chitosan adsorption capabilities.

Figures S11a,b (Supporting Information) illustrate the appearance of the sponges before and after dye removal, along with the corresponding water solutions (Figures S11d,e, Supporting Information). The dye (Direct Blue-78) was uniformly distributed on the surface of the sponge, which turned dark blue, indicating effective dye removal from the water. Adsorption appeared to begin on the external surface and progressed toward the core of the sponge through diffusion.

In contrast, the pristine chitosan sponge, after 15 min of dye contact, swelled considerably, as shown in Figure S11b (Supporting Information), with minimal dye adsorption. After 60 min, it dissolved completely. The maximum adsorption capacity (q_{max}) for the ALD ZnO-modified sponges reached up to 2000 mg g^{-1}—a remarkably high value compared to similar studies reported in the literature.[22,94–96] We suppose that the ALD ZnO layer made the polymer more rigid, as witnessed by FT-IR, and hydrophobic, increasing the affinity toward DB that appeared macroscopically more uniformly distributed on both faces of the sponges. The wettability measurements pointed out that ZnO thin films deposited onto silicon were hydrophobic showing a water contact angle of 94° ± 4°, corroborating this hypothesis. At the same time, the presence of electrostatic forces enhanced the process. Indeed, the molecular structure of DB, reported in Figure 7a, depicts the presence of sulfonate groups that are likely deprotonated in the adopted experimental conditions, being characterized by pKa < 2. Hence, DB could also interact with positively charged chitosan chains as already reported in previous works.[93] However, to get more insight into the nature of the interaction, ATR-FT-IR analyses were performed after DB adsorption (Figures S12a,b, Supporting Information).

The pristine sponges and ZnO(50 cycles)@Chitosan samples were taken as case studies. The DB ATR-FT-IR spectrum was also collected to highlight its slight contribution in the composite material, due to its small amount. The spectrum showed the typical features of azo dyes, already described in the literature, but not significantly detected in the composite material.[91] Thus, the observed changes could be referred to as the main chitosan vibration modes, and are comparable on both faces of the sponge, denoting the uniform distribution of the color, as also appreciated macroscopically.

After the DB adsorption, the wavenumber region 2000–1000 cm^{-1} of the chitosan spectrum was found greatly affected, and all bands reduced their relative intensity and ratio, indicating a hydrogen bonding reorganization. Specifically, the signal at 1410 cm^{-1} reduced its relative intensity and, at the same time, the C—O—C vibration modes slightly changed. Additionally, the OH and NH stretching band intensity was found weak, and the band less defined. Moreover, due to the changes referred to amide I and II, the involvement of amino groups during the interaction with the adsorbate was thus undoubtedly confirmed, and accordingly, the C—N signal shifted from 1378 to 1370 cm^{-1}.[91]

The obtained results highlighted the potential of the proposed materials, opening a new horizon in the use of innovative water remediation approaches.

3.6. Preliminary Evaluation of the Photocatalytic Properties and Product Analysis

To evaluate the photocatalytic properties of the developed sponges, experiments were conducted using Naproxen (NAX), a well-known pharmaceutical compound classified as an emerging pollutant. Notably, NAX is not adsorbed by chitosan sponges, making it an ideal candidate to specifically assess the photocatalytic activity of ZnO under UV light conditions.[97] For this study, ZnO-coated chitosan sponges with 50 ALD cycles [ZnO(50 cy)@Chitosan] were immersed in water containing 10 mg L^{-1} of NAX.

Previous studies, such as those by Štrbac et al., have demonstrated that ZnO effectively degrades NAX, showing superior performance compared to TiO_2.[98,99] Therefore, our experiments aimed to verify if the catalytic properties of ZnO were retained in the ALD-modified sponges.

To monitor NAX degradation, the absorbance of the solution was measured, focusing on its prominent UV absorption band at 225 nm (see **Figure 8**).

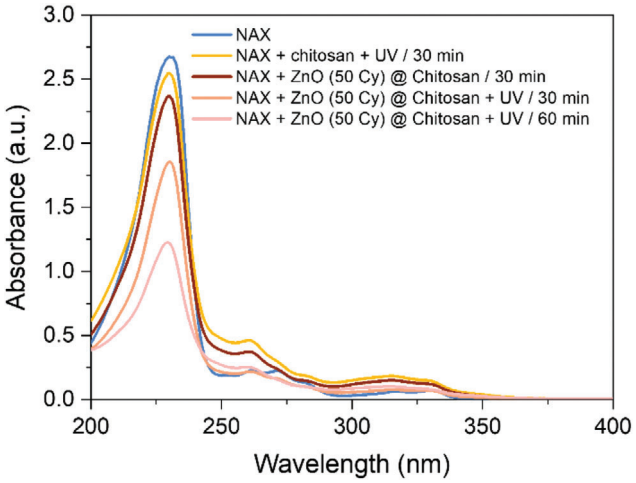

Figure 8. A comparison between UV–vis spectra of NAX solutions under different conditions of work, showing the effective photocatalysis of ALD-modified chitosan sponges.

Initially, a control experiment was performed to confirm the minimal adsorption of NAX onto both the pristine chitosan and ZnO-modified sponges (see Figure S13, Supporting Information, up to 240 min). Subsequently, the NAX solution was exposed to UV light in the presence of either the pristine chitosan sponge or the ZnO-modified sponge. After 30 and 60 min of irradiation, a significant decrease in the absorbance was observed only with the ZnO-modified sponges, indicating effective photocatalytic activity. In contrast, when exposed to UV light with the pristine chitosan sponge alone, NAX underwent minimal photodegradation. These results confirm that the reduction in NAX concentration is attributable to the photocatalytic action of ZnO rather than to adsorption.

Furthermore, a preliminary analysis of the photocatalytic products was performed to further confirm the effectiveness of the photocatalytic system. The acquired chromatograms (Figure S14, Supporting Information) of samples collected at 0, 2, and 4 h of UV exposure in the presence of ZnO-coated sponges showed multiple new peaks increasing in intensity over time (Figure S15, Supporting Information), relative to the initial sample (time zero). Table S2 (Supporting Information) lists the calculated and measured accurate masses, predicted formulas, mass errors, and MS/MS data for the 11 detected Naproxen photo products.

For each potential photoproduct, the proposed structure was deduced by interpreting the accurate mass, isotopic pattern, and high-resolution MS/MS data. Furthermore, the identification was validated by comparing the detected peaks to a list of major photoproducts previously reported in the literature for Naproxen photodegradation, including those catalyzed by metal oxides. These results confirm the functionality and effectiveness of the nanoengineered sponges in photocatalytic applications.[100–108]

These findings demonstrate that ZnO(50 cy)@Chitosan sponges are effective in degrading non-adsorbing pollutants, underscoring their potential for water remediation applications. The synergistic action of ZnO and UV light enhances the utility of these nanoengineered sponges in treating contaminated water.

4. Conclusion

In this study, highly efficient ALD-nanoengineered chitosan/ZnO sponges were successfully developed and investigated for pollutant removal via physical adsorption and solid-state photocatalysis, serving as a proof of concept. Initially, thin chitosan films were prepared as model systems to evaluate the growth quality and opto-chemical properties of ZnO as a function of the ALD cycle number. These findings were further confirmed and detailed when applied to porous chitosan sponges. Notably, subsurface infiltration of ZnO was observed in the thin films, with penetration depths reaching up to tens of nanometers. Within the sponge matrix, the ZnO growth extended to several hundred microns, indicative of a reaction-limited growth process.

The ALD-grown ZnO on chitosan was found to be amorphous, exhibiting defect-related photoluminescence in the red region. XPS analysis highlighted the chemisorptive role of protonated amine groups in the interaction with the ALD Zn precursor, especially within the chitosan sponge matrix. The adsorption capabilities of these nanoengineered sponges were evaluated using Direct Blue-78, a commonly used textile dye, as a model contaminant. The adsorption process was monitored through UV–vis and ATR-FT-IR spectroscopy, revealing significantly enhanced dye removal compared to pristine chitosan sponges.

Moreover, preliminary UV–vis and product analysis experiments demonstrated that the modified sponges are photocatalytically active, effectively degrading emerging contaminants such as Naproxen under light exposure. These results suggest that ALD is a promising technique for creating nanoengineered chitosan-based adsorbents for water remediation, providing a novel approach to surface modification that has not been extensively explored. This study paves the way for the development of multifunctional, sustainable materials for environmental applications, combining adsorption and photocatalysis for the effective removal of a wide range of water pollutants.

Supporting Information

Supporting Information is available from the Wiley Online Library or from the author.

Acknowledgements

The authors thank S. Cosmai and D. Benedetti for their technical support. This work was supported by the European Union – Next Generation EU, in the framework of the National Recovery and Resilience Plan, Mission 4, Component 2, with the project BECOMEH2 (CUP B53D23027360001).

Open access publishing facilitated by Consiglio Nazionale delle Ricerche, as part of the Wiley - CRUI-CARE agreement.

Conflict of Interest

The authors declare no conflict of interest.

Data Availability Statement

The data that support the findings of this study are available from the corresponding author upon reasonable request.

Keywords

atomic layer deposition (ALD), chitosan, photocatalysis, water remediation, ZnO

Received: October 19, 2024
Revised: December 17, 2024
Published online:

[1] A. D. Plessis, *Springer Water Water as an Inescapable Risk Current Global Water Availability, Quality and Risks with a Specific Focus on South Africa*, Springer, Berlin, Germany **2019**.
[2] I. C. Vasilachi, D. M. Asiminicesei, D. I. Fertu, M. Gavrilescu, *Water* **2021**, *13*, 181.
[3] V. Geissen, H. Mol, E. Klumpp, G. Umlauf, M. Nadal, M. van der Ploeg, S. E. A. T. M. van de Zee, C. J. Ritsema, *Int. Soil and Water Conserv. Res.* **2015**, *3*, 57.
[4] M. O. Barbosa, N. F. F. Moreira, A. R. Ribeiro, M. F. R. Pereira, A. M. T. Silva, *Water Res.* **2016**, *94*, 257.
[5] M. Mofijur, M. M. Hasan, S. F. Ahmed, F. Djavanroodi, I. M. R. Fattah, A. S. Silitonga, M. A. Kalam, J. L. Zhou, T. M. Y. Khan, *Environ. Pollution* **2024**, *341*, 122889.
[6] M. R. Adam, M. H. D. Othman, T. A. Kurniawan, M. H. Puteh, A. F. Ismail, W. Khongnakorn, M. A. Rahman, J. Jaafar, *J. Environ. Chem. Eng.* **2022**, *10*, 107633.
[7] M. R. Awual, M. M. Hasan, J. Iqbal, M. A. Islam, A. Islam, S. Khandaker, A. M. Asiri, M. M. Rahman, *J. Environ. Chem. Eng.* **2020**, *8*, 103591.
[8] M. R. Awual, N. H. Alharthi, M. M. Hasan, M. R. Karim, A. Islam, H. Znad, M. A. Hossain, M. E. Halim, M. M. Rahman, M. A. Khaleque, *Chem. Eng. J.* **2017**, *324*, 130.
[9] M. R. Awual, *J. Environ. Chem. Eng.* **2019**, *7*, 103124.
[10] M. N. Hasan, M. A. Shenashen, M. M. Hasan, H. Znad, M. R. Awual, *Chemosphere* **2021**, *270*, 128668.
[11] M. R. Awual, *Chem. Eng. J.* **2016**, *300*, 264.
[12] M. S. Salman, M. C. Sheikh, M. M. Hasan, M. N. Hasan, K. T. Kubra, A. I. Rehan, M. E. Awual, A. I. Rasee, R. M. Waliullah, M. S. Hossain, M. A. Khaleque, A. K. D. Alsukaibi, H. M. Alshammari, Md. R. Awual, *Appl Surf Sci* **2023**, *622*, 157008.
[13] R. M. Waliullah, A. I. Rehan, M. E. Awual, A. I. Rasee, M. C. Sheikh, M. S. Salman, M. S. Hossain, M. M. Hasan, K. T. Kubra, M. N. Hasan, H. M. Marwani, A. Islam, M. M. Rahman, M. A. Khaleque, M. R. Awual, *J. Mol. Liq.* **2023**, *388*, 122763.
[14] K. T. Kubra, M. M. Hasan, M. N. Hasan, M. S. Salman, M. A. Khaleque, M. C. Sheikh, A. I. Rehan, A. I. Rasee, R. M. Waliullah, M. E. Awual, M. S. Hossain, A. K. D. Alsukaibi, H. M. Alshammari, M. R. Awual, *Colloids Surf. A Physicochem. Eng. Asp.* **2023**, *667*, 131415.
[15] M. R. Awual, M. N. Hasan, M. M. Hasan, M. S. Salman, M. C. Sheikh, K. T. Kubra, M. S. Islam, H. M. Marwani, A. Islam, M. A. Khaleque, R. M. Waliullah, M. S. Hossain, A. I. Rasee, A. I. Rehan, M. E. Awual, *Sep. Purif. Technol.* **2023**, *319*, 124088.
[16] A. Islam, S. H. Teo, Y. H. Taufiq-Yap, C. H. Ng, D.-V. N. Vo, M. L. Ibrahim, M. M. Hasan, M. A. R. Khan, A. S. M. Nur, Md. R. Awual, *Resour. Conserv. Recycl.* **2021**, *175*, 105849.
[17] H. M. Munjur, M. N. Hasan, M. R. Awual, M. M. Islam, M. A. Shenashen, J. Iqbal, *J. Mol. Liq.* **2020**, *319*, 114356.
[18] M. R. Awual, M. M. Hasan, A. M. Asiri, M. M. Rahman, *Compos. B Eng.* **2019**, *171*, 294.
[19] K. T. Kubra, M. S. Salman, H. Znad, M. N. Hasan, *J. Mol. Liq.* **2021**, *329*, 115541.
[20] A. Shahat, K. T. Kubra, M. S. Salman, M. N. Hasan, M. M. Hasan, *Microchem. J.* **2021**, *164*, 105967.
[21] E. Salehi, M. Khajavian, N. Sahebjamee, M. Mahmoudi, E. Drioli, T. Matsuura, *Desalination* **2022**, *527*, 115565.
[22] A. Murcia-Salvador, J. A. Pellicer, M. I. Fortea, V. M. Gómez-López, M. I. Rodríguez-López, E. Núñez-Delicado, J. A. Gabaldón, *Polymers (Basel)* **2019**, *11*, 1003.
[23] M. Malini, M. Thirumavalavan, W. Y. Yang, J. F. Lee, G. Annadurai, *Int. J. Biol. Macromol.* **2015**, *80*, 121.
[24] H. Shehzad, E. Ahmed, A. Sharif, Z. H. Farooqi, M. I. Din, R. Begum, Z. Liu, L. Zhou, J. Ouyang, A. Irfan, I. Nawaz, *Int. J. Biol. Macromol.* **2022**, *194*, 117.
[25] R. Gajera, R. V. Patel, A. Yadav, P. K. Labhasetwar, *J. Water Process Eng.* **2022**, *49*, 102993.
[26] H. Hassan, A. Salama, A. K. El-ziaty, M. El-Sakhawy, *Int. J. Biol. Macromol.* **2019**, *131*, 520.
[27] O. A. Attallah, M. Rabee, *RSC Adv.* **2020**, *10*, 40697.
[28] K. M. Lee, C. W. Lai, K. S. Ngai, J. C. Juan, *Water Res.* **2016**, *88*, 428.
[29] I. Aadnan, O. Zegaoui, I. Daou, J. C. G. Esteves da Silva, *J. Environ. Chem. Eng.* **2020**, *8*, 104260.
[30] E. E. Elemike, D. C. Onwudiwe, J. I. Mbonu, *J. Inorg. Organomet. Polym. Mater.* **2021**, *31*, 3356.
[31] B. Gupta, A. K. Gupta, *Int. J. Biol. Macromol.* **2022**, *198*, 87.
[32] X. Yang, A. B. F. Martinson, J. W. Elam, L. Shao, S. B. Darling, *Matter* **2021**, *4*, 3515.
[33] M. Weber, A. Julbe, A. Ayral, P. Miele, M. Bechelany, *Chem. Mater.* **2018**, *30*, 7368.
[34] R. Li, N. Li, J. Hou, Y. Yu, L. Liang, B. Yan, G. Chen, *J. Hazard. Mater.* **2021**, *402*, 123513.
[35] M. Weber, A. Julbe, S. S. Kim, M. Bechelany, *J. Appl. Phys.* **2019**, *126*, 041101.
[36] B. Jeong, D. H. Kim, E. J. Park, M. G. Jeong, K. D. Kim, H. O. Seo, Y. D. Kim, S. Uhm, *Appl. Surf. Sci.* **2014**, *307*, 468.
[37] M. E. Fragalà, A. Di Mauro, D. A. Cristaldi, M. Cantarella, G. Impellizzeri, V. Privitera, *J. Photochem. Photobiol. A. Chem.* **2017**, *332*, 497.
[38] N. Li, J. Zhang, Y. Tian, J. Zhao, J. Zhang, W. Zuo, *Chem. Eng. J.* **2017**, *308*, 377.
[39] T. E. Berger, C. Regmi, A. I. Schäfer, B. S. Richards, *J Memb. Sci.* **2020**, *604*, 118015.
[40] Y. Q. Cao, T. Q. Zi, X. R. Zhao, C. Liu, Q. Ren, J. Bin Fang, W. M. Li, A. D. Li, *Sci. Rep.* **2020**, *10*, 13437.
[41] D. P. Gaillot, O. Deparis, V. Welch, B. K. Wagner, J. P. Vigneron, C. J. Summers, *Phys. Rev. E. Stat. Nonlin. Soft. Matter. Phys.* **2008**, *78*, 031922.
[42] B. Boury, S. Plumejeau, *Green Chem.* **2014**, *17*, 72.
[43] L. Angelova, I. Bliznakova, A. Daskalova, B. Blagoev, A. Trifonov, P. Terziyska, I. Buchvarov, *Opt. Quantum Electron* **2020**, *52*, 173.
[44] Y. Zhu, X. Liu, K. W. K. Yeung, P. K. Chu, S. Wu, *Appl. Surf. Sci.* **2017**, *400*, 14.
[45] T. Hirvikorpi, M. Vähä-Nissi, A. Harlin, M. Salomäki, S. Areva, J. T. Korhonen, M. Karppinen, *Appl. Surf. Sci.* **2011**, *257*, 9451.
[46] V. Rizzi, F. Romanazzi, J. Gubitosa, P. Fini, R. Romita, A. Agostiano, A. Petrella, P. Cosma, *Biomolecules* **2019**, *9*, 571.
[47] M. Wang, Y. Ma, Y. Sun, S. Y. Hong, S. K. Lee, B. Yoon, L. Chen, L. Ci, J. Do Nam, X. Chen, J. Suhr, *Sci. Rep.* **2017**, *7*, 18054.
[48] M. Zeng, W. Wu, J. Fang, S. Li, Z. Zhou, *J. Mater. Sci.* **2019**, *54*, 9995.
[49] M. Wang, Y. Ma, Y. Sun, S. Y. Hong, S. K. Lee, B. Yoon, L. Chen, L. Ci, J.-D. Nam, X. Chen, J. Suhr, *Sci. Rep.* **2017**, *7*, 18054.
[50] J. Pilz, M. Tazreiter, A. M. Coclite, *J. Vac. Sci. Technol., A* **2019**, *37*, 063201.
[51] J. Gubitosa, V. Rizzi, P. Fini, F. Fanelli, T. Sibillano, N. Corriero, P. Cosma, *J. Mater. Chem. B* **2023**, *11*, 2638.
[52] J. Gubitosa, V. Rizzi, D. Cignolo, P. Fini, F. Fanelli, P. Cosma, *Sustain. Chem. Pharm.* **2022**, *29*, 100749.

[53] V. Rizzi, J. Gubitosa, P. Fini, A. Petrella, R. Romita, A. Agostiano, P. Cosma, *Environ. Technol. Innov.* **2020**, *19*, 100812.
[54] W. L. Bond, *J. Appl. Phys.* **1965**, *36*, 1674.
[55] M. J. Zhao, Z. T. Sun, C. H. Hsu, P. H. Huang, X. Y. Zhang, W. Y. Wu, P. Gao, Y. Qiu, S. Y. Lien, W. Z. Zhu, *Nanomaterials* **2020**, *10*, 459.
[56] J. Pilz, A. Perrotta, G. Leising, A. M. Coclite, *Physica Status Solidi (A) Appl. Mater. Sci.* **2020**, *217*, 1900256.
[57] V. Srikant, D. R. Clarke, *J. Appl. Phys.* **1998**, *83*, 5447.
[58] B. D. Viezbicke, S. Patel, B. E. Davis, D. P. Birnie, *Phys. Status Solidi B Basic Res.* **2015**, *252*, 1700.
[59] E. Ş. Tüzemen, S. Eker, H. Kavak, R. Esen, *Appl. Surf. Sci.* **2009**, *255*, 6195.
[60] J. Pilz, A. Perrotta, P. Christian, M. Tazreiter, R. Resel, G. Leising, T. Griesser, A. M. Coclite, *J. Vac. Sci. Technol., A* **2018**, *36*, 01A109.
[61] L. Fang, H. Li, X. Ma, Q. Song, R. Chen, *Appl. Surf. Sci.* **2020**, *527*, 146818.
[62] R. C. Rai, *J. Appl. Phys.* **2013**, *113*, 153508.
[63] D. Saha, A. K. Das, R. S. Ajimsha, P. Misra, L. M. Kukreja, *J. Appl. Phys.* **2013**, *114*, 146818.
[64] A. Perrotta, J. Pilz, S. Pachmajer, A. Milella, A. M. Coclite, *Beilstein J. Nanotechnol.* **2019**, *10*, 746.
[65] M. C. Biesinger, L. W. M. Lau, A. R. Gerson, R. S. C. Smart, *Appl. Surf. Sci.* **2010**, *257*, 887.
[66] Y. Du, M. S. Zhang, J. Hong, Y. Shen, Q. Chen, Z. Yin, *Appl. Phys. A Mater. Sci. Process* **2003**, *76*, 171.
[67] L. W. Lai, C. T. Lee, *Mater. Chem. Phys.* **2008**, *110*, 393.
[68] S. Y. Pung, K. L. Choy, X. Hou, C. Shan, *Nanotechnology* **2008**, 435609, *19*.
[69] A. Di Mauro, M. Cantarella, G. Nicotra, V. Privitera, G. Impellizzeri, *Appl. Catal. B* **2016**, *196*, 68.
[70] A. Djelloul, M. S. Aida, J. Bougdira, *J. Lumin.* **2010**, *130*, 2113.
[71] S. I. Boyadjiev, V. Georgieva, R. Yordanov, Z. Raicheva, I. M. Szilágyi, *Appl. Surf. Sci.* **2016**, *387*, 1230.
[72] A. Srivastava, M. Arora, S. Gupta, B. Chakraborty, S. Chandra, S. Toyoda, H. Bahadur, *J. Mater. Sci. Techno.* **2010**, *26*, 986.
[73] C. Z. Leng, M. D. Losego, *Mater. Horiz.* **2017**, *4*, 747.
[74] E. Cara, I. Murataj, G. Milano, N. De Leo, L. Boarino, F. F. Lupi, *Nanomaterials* **2021**, *11*, 994.
[75] C. A. Wilson, R. K. Grubbs, S. M. George, *Chem. Mater.* **2005**, *17*, 5625.
[76] L. H. Li, J. C. Deng, H. R. Deng, Z. L. Liu, L. Xin, *Carbohydr. Res.* **2010**, *345*, 994.
[77] R. Kubo, *J. Phys. Soc. Jpn.* **1962**, *17*, 975.
[78] D. Mora-Fonz, A. L. Shluger, *Adv. Electron. Mater.* **2020**, *6*, 1900760.
[79] L. Demelius, M. Blatnik, K. Unger, P. Parlanti, M. Gemmi, A. M. Coclite, *Appl. Surf. Sci.* **2022**, *604*, 154619.
[80] V. Rizzi, P. Fini, F. Fanelli, T. Placido, P. Semeraro, T. Sibillano, A. Fraix, S. Sortino, A. Agostiano, C. Giannini, P. Cosma, *Food Hydrocoll* **2016**, *58*, 98.
[81] Y. S. Min, C. J. An, S. K. Kim, J. Song, C. S. Hwang, *Bull. Korean Chem. Soc.* **2010**, *31*, 2503.
[82] T. L. Barr, S. Seal, *J. Vac. Sci. Technol., A* **1995**, *13*, 1239.
[83] K. J. Qian, S. Chen, B. Zhu, L. Chen, S. J. Ding, H. L. Lu, Q. Q. Sun, D. W. Zhang, Z. Chen, *Appl. Surf. Sci.* **2012**, *258*, 4657.
[84] J. F. Moulder, W. F. Stickle, P. E. Sobol, K. D. Bomben, *Handbook of X-Ray Photoelectron Spectroscopy*, Perkin-Elmer, Eden Prairie, MN, **1992**, p. 2002.
[85] G. Lawrie, I. Keen, B. Drew, A. Chandler-Temple, L. Rintoul, P. Fredericks, L. Grøndahl, *Biomacromolecules* **2007**, *8*, 2533.
[86] H. Maachou, M. J. Genet, D. Aliouche, C. C. Dupont-Gillain, P. G. Rouxhet, *Surf. Interface Anal.* **2013**, *45*, 1088.
[87] I. Perelshtein, E. Ruderman, N. Perkas, T. Tzanov, J. Beddow, E. Joyce, T. J. Mason, M. Blanes, K. Mollá, A. Patlolla, A. I. Frenkel, A. Gedanken, *J. Mater. Chem. B* **2013**, *1*, 1968.
[88] W. Wang, C. Chen, C. Tollan, F. Yang, M. Beltrán, Y. Qin, M. Knez, *ACS Appl. Mater. Interfaces* **2017**, *9*, 27964.
[89] W. Szmyt, C. Guerra-Nuñez, L. Huber, C. Dransfeld, I. Utke, *Chem. Mater.* **2022**, *34*, 203.
[90] X. Qu, A. Wirsén, A. C. Albertsson, *Polymer (Guildf)* **2000**, *41*, 4589.
[91] V. Rizzi, A. Longo, T. Placido, P. Fini, J. Gubitosa, T. Sibillano, C. Giannini, P. Semeraro, E. Franco, M. Ferrandiz, P. Cosma, *J. Appl. Polym. Sci.* **2018**, *135*, 45945.
[92] V. Rizzi, J. Gubitosa, P. Fini, S. Nuzzo, P. Cosma, *Sustain. Mater. Technol.* **2020**, *26*, e00231.
[93] V. Rizzi, F. Fiorini, G. Lamanna, J. Gubitosa, E. A. Prasetyanto, P. Fini, F. Fanelli, A. Nacci, L. De Cola, P. Cosma, *Adv. Sustain. Syst.* **2018**, *2*, 1700146.
[94] M. M. H. Elzahar, M. Bassyouni, *Sci. Rep.* **2023**, *13*, 15750.
[95] M. B. Wazir, M. Daud, F. Ali, M. A. Al-Harthi, *J. Mol. Liq.* **2020**, *315*, 113775.
[96] J. Gubitosa, V. Rizzi, P. Fini, S. Nuzzo, P. Cosma, *Phys. Chem. Chem. Phys.* **2024**, *26*, 9891.
[97] M. Baratta, A. Tursi, M. Curcio, G. Cirillo, A. V. Nezhdanov, A. I. Mashin, F. P. Nicoletta, G. De Filpo, *Molecules* **2022**, *27*, 7674.
[98] D. Štrbac, C. A. Aggelopoulos, G. Štrbac, M. Dimitropoulos, M. Novaković, T. Ivetić, S. N. Yannopoulos, *Process Saf. Environ. Prot.* **2018**, *113*, 174.
[99] R. Sabouni, H. Gomaa, *Environ. Sci. Pollut. Res.* **2019**, *26*, 5372.
[100] G. Hemanathan, S. Karthikeyan, R. Kathirvel, *Desalin. Water Treat* **2024**, *320*, 100675.
[101] F. Méndez-Arriaga, J. Gimenez, S. Esplugas, *J. Adv. Oxi. Technol.* **2008**, *11*, 2008.
[102] D. Kanakaraju, C. A. Motti, B. D. Glass, M. Oelgemöller, *Chemosphere* **2015**, *139*, 579.
[103] N. Jallouli, K. Elghniji, O. Hentati, A. R. Ribeiro, A. M. T. Silva, M. Ksibi, *J. Hazard. Mater.* **2016**, *304*, 329.
[104] S. Gong, C. Ding, J. Liu, K. Fu, Y. Pan, J. Shi, H. Deng, *Chem. Eng. J.* **2022**, *430*, 133016.
[105] E. Aydin, *Clean (Weinh)* **2015**, *43*, 59.
[106] R. Marotta, D. Spasiano, I. Di Somma, R. Andreozzi, *Water Res.* **2013**, *47*, 373.
[107] E. Arany, R. K. Szabó, L. Apáti, T. Alapi, I. Ilisz, P. Mazellier, A. Dombi, K. Gajda-Schrantz, *J. Hazard. Mater.* **2013**, *262*, 151.
[108] X. Li, Y. Cai, J. Chen, J. Lu, J.-M. Chovelon, Q. Zhou, Y. Ji, *J. Hazard. Mater.* **2024**, *474*, 134841.